UNSTEADY CONJUGATE HEAT TRANSFER MEASUREMENTS IN THE PRESENCE OF LATERAL CONDUCTION

S. Brack, R. Poser and J. von Wolfersdorf

Institute of Aerospace Thermodynamics (ITLR),
University of Stuttgart,
Germany

Keywords: unsteady heat transfer, lateral conduction, hot-wire anemometry, infrared thermography

ABSTRACT

An experimental setup for unsteady heat transfer experiments is presented and characterized. Inside a Perspex test section the fluid velocity and temperature vary independently of each other with the aid of an electric throttle mechanism and an electric mesh heater. Both fluid quantities are temporally resolved with hot wire probes and fluid thermocouples. The independent control of the fluid velocity and the fluid temperature is achieved by the calculation of the control variable histories before each experiment. Therefore, a measurement of the operational range of the experimental setup is performed. The measurement of the inlet velocity profiles verified a deterministic boundary condition for the unsteady heat transfer experiments.

The application of an in situ calibrated infrared camera delivers spatially and temporally resolved surface temperatures which are evaluated to get spatially and temporally resolved heat flux patterns. An evolution algorithm provides an automatic assignment of infrared camera pixels to the thermocouple response.

The operability of the experimental setup and the evaluation method is discussed by presenting two experimental results of an unsteady heat transfer situation in the wake region of a vortex generator. The first experiment was performed with a sinusoidal variation of the fluid temperature and a constant fluid velocity. Within the second experiment, the heat transfer gets unsteady induced by a sinusoidal variation of the fluid speed and a temporarily constant fluid temperature.

NOMENCLATURE

Acronyms
CCT   Constant current thermometry
CTA   Constant temperature anemometry
DL   Digital level (quantity of the IRT camera)
IRT   Infrared thermography

Greek symbols
ΔT Temperature difference
Δx Distance
ρ Density
Ω Vane angle
θ Normalized temperature
σ Standard deviation

Roman symbols
a Thermal diffusivity
Bi   Biot number
c Specific heat capacity
d Diameter
h Heat transfer coefficient
k Thermal conductivity
L Plate thickness
$\dot{m}$ Mass flow
p Pressure
P Power
$\dot{q}$ Heat flux
$\Re$ Specific gas constant for an ideal gas
R Resistance
Re   Reynolds number
T Temperature
Tu   Turbulence intensity
U Voltage
u Velocity
t Time
u, v, w Frequencies
x, y, z Coordinate

Subscripts
0   Initial
C   Channel
d   Duration
f   Fluid
H   Heater
ref   Reference
s   Surface
STC   Surface thermocouple
u Velocity
w   Wall
∞ Ambient

Superscripts
$\bar{x}$ Average value
$\tilde{x}$ Fourier transform

INTRODUCTION

Internal turbine cooling systems are described by complex heat transfer patterns as a result of their geometrical shape with, for example, skewed ribs, impingement cooling or film cooling [1]. Further, these cooling systems are often exposed to temporally varying thermal boundary conditions during operation. Causes for such temporal variations are, for example, the working principle, changing operation points or stochastic processes like combustion instabilities.

These temporal variations in the fluid ty u, the fluid temperature T_f or the heat load cause temporal variations of transferred surface heat flux $\dot{q}_s$, the surface temperature T_s as well as the solid temperatures. Also the heat transfer coefficient

$$h = \frac{\dot{q}_s}{T_{ref} - T_s},\qquad(1)$$

defined by the Newton's law of cooling, may be a time-dependent quantity [2-4].

For unsteady heat transfer phenomena, in particular, the material properties (k_w, ρ_w, c_w) and the dimensions of the participated wall can influence the heat exchange. The temporal changes on the fluid side cause heat conduction processes influencing the heat transfer process itself [2,3].

As a consequence of its importance and complexity, it is of interest to investigate and capture such unsteady heat transfer phenomena experimentally. Former experimental investigations focused on periodic variations of the fluid temperature or the fluid velocity comparing the temporally averaged heat transfer with steady heat transfer situations. Especially in the case of fluid velocity pulsation, the research results show no clear trend and contradicting findings concerning possible heat transfer augmentation effects [3,5].

Many researchers investigated the effects of unsteady heat transfer with on the one hand local and on the other hand temporally averaged measurements. For example, Dec and Keller [6] studied the heat transfer characteristics in a pulsating pipe flow (fluid velocity) with surface thermocouples, wall thermocouples and fluid thermocouples. First, the measurements were temporally averaged. Then the surface heat flux was calculated with the approximated Fourier's law

$$\dot{q} = k_w \frac{\Delta T}{\Delta x},\qquad(2)$$

using the temperature difference ΔT and the distance Δx between surface and wall thermocouple. Equation (1) delivered the local heat transfer coefficient.

Ishino et al. [7] also resolved the unsteady heat transfer for pulsating fluid velocity with temporally averaged surface thermocouple measurements and a constant outer wall temperature boundary condition. Further an energy balance evaluation method

delivered area and temporally averaged heat transfer coefficients using the temporally averaged T_f results at different axial positions.

In contrast to the temporally averaged heat transfer investigations, Barker and Williams [8] temporally resolved the transient response of the heat transfer coefficient with a local heat flux sensor imbedded in the wall and exposed to a pulsing fluid velocity channel flow.

Also Liu et al. [9-11] investigated the temporally resolved unsteady heat transfer over a flat plate with flush-mounted surface thermocouples. Laminar and turbulent regimes as well as fluid velocity pulsation and fluid temperature pulsation were investigated.

For complex heat transfer situations like impingement cooling or film cooling, thermocouple arrays are a common approach to measure the surface temperature at several local positions. The applied evaluation methods are the same as discussed above [12, 13].

Apart from the local heat transfer measurements, some investigations were conducted with spatially resolved surface temperature measurement techniques. For example, Hofmann et al. [15], Coulthard et al. [16] and Ekkad et al. [5] acquired temporally averaged surface temperatures with an infrared camera for impingement cooling and film cooling configurations with pulsating flows.

Temporally and spatially resolved unsteady heat transfer data is still very scarce. Therefore, this paper presents an experimental setup to spatially and temporally resolve complex heat transfer patterns during unsteady thermal boundary conditions. In a first step, the experimental approaches including the test facility, the necessary determination of the operational range and an approach to improve the in situ calibration of the infrared camera are discussed. In a second step, the applied evaluation method for complex and unsteady heat transfer patterns and its limitations are elaborated. In a third step, the results of two different unsteady heat transfer situations in the wake region of a vortex generator are presented. One experiment was performed with a constant fluid velocity and a pulsating fluid temperature. During the second experiment the fluid velocity pulsates and the fluid temperature is kept constant within different time intervals.

EXPERIMENTAL APPROACHES

This section splits up into the parts experimental setup, operational range, boundary velocity profiles and in situ calibration. The first parts presents the components, the geometrical dimensions and the general working principle of the experimental setup which is a further development of the setup designed by Liu et al. [9]. Within the second part further details about the operational range and its application to calculate the control variable in ad-
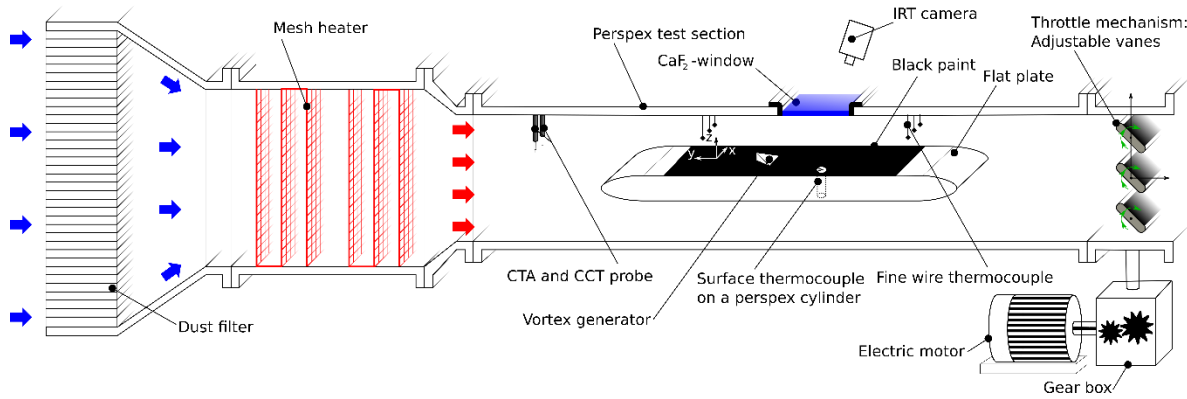
Figure 1: Experimental Setup

vance are given. The variation of the inlet velocity profiles
during operation are discussed in part three and at the end an approach to improve the in situ calibration of the infrared camera is presented.

The experimental setup, shown in Fig. 1, is designed to perform unsteady conjugate heat transfer experiments with an independent control of u and T_f. In order to achieve this, a Pfeiffer WGK8000 roots vacuum pump sucks air with a constant flow rate through the complete experimental setup consisting of a dust filter followed by a mesh heater, the Perspex test section and adjustable vanes at the end. Varying on the one hand the heater voltage U_H and on the other hand the constriction at the throttle mechanism by changing the angle of attack of the vanes Ω, leads to a certain u and T_f inside the test section. Further details about relationship between (U_H, Ω) and (u, T_f) are given in the second part of this section.

The fluid velocity u and the fluid temperature T_f, used to describe the conditions inside the Perspex test section, are locally measured 0.205 m in front and 0.020 m above of the flat plate. The suitability of the measurement position to represent the fluid conditions inside the test section is shown in the third part of this section.

Two previously calibrated 10 μm hot wire probes operating in constant temperature mode (CTA) and constant current mode (CCT) measure u and T_f variations up to a frequency of 5 kHz. With the aid of the CCT measurements, the influence of a varying fluid temperature on the CTA signal is compensated. The applied SVMtec hot wire 4CTA system includes the measuring circuit and the NI-USB6211 data acquisition device.

Before each experiment, the general flow velocity level is set on the one hand with the rotational speed of the roots vacuum pump (15 Hz to 60 Hz). On the other hand the flow through an additional bypass duct can be controlled with an adjustable valve.

Apart from the general flow velocity level set before the experiment, the fluid velocity variations during the experiment are mainly controlled by the throttle mechanism. Therefore three vanes, arranged above one another, change their angle of attack Ω. The vanes have a wingspan of 0.12 m and a chord length of 0.049 m. This vane dimensions lead to a minimum gap of $10 \cdot 10^{-4}$ m between the vanes and $5 \cdot 10^{-4}$ m between a vane and the lower or upper wall.

A Kübler 5850 absolute shaft encoder measures the current Ω which is further used as the process quantity of a PI controller setting the rotational speed of the VEM asynchronous motor.

Figure 2 visualizes the definition of Ω. An angle of attack Ω of 90 ° represents the minimum opening position with the slowest u. The initial output angle of the shaft encoder can differ from Ω. Therefore, a reference run with constant rotational speed sweeping across at least 200 ° delivers the previously not known $\Omega = 90$ ° position. Figure 3 shows the velocity measured during a reference run and illustrates the sharp minima of u.

The nonlinear dependence between u and Ω is visualized in Fig. 4. For larger angles of attack Ω the slope of u decreases which makes fast adjustments of u more difficult. For this reason, the used Ω was restricted to the angular range of 90 °-140 °.

Two Munk PSP varipuls switch-mode AC power supply units provide a maximum output of 9.75 kW and power three fine wire meshes each. The meshes are arranged downstream of each other and ensure a homogeneous temperature distribution over the complete cross section. In addition, the low thermal mass of the meshes ($m_H c_H$) results in a fast response to variations. An external control voltage is used to modify the power during operation.

The Perspex test section ($\rho_w = 1190$ kg/m^3, $c_w = 1470$ J/kgK, $k_w = 0.19$ W/mK) of the experimental setup consists of a channel with a rectangular cross-section area of 0.12x0.15 m^2. A 0.03 m thick (L) flat plate is placed in the symmetry plane of the channel and a vortex generator

is mounted on top. The central location of the vortex generator is 0.29 m downstream of the elliptical leading edge and leads to a longitudinal vortex system discussed in detail by Henze et al. [17]. A strong vortex system is guaranteed by the dimensions of the vortex generator (0.026 m high and 0.065 m wide and long).
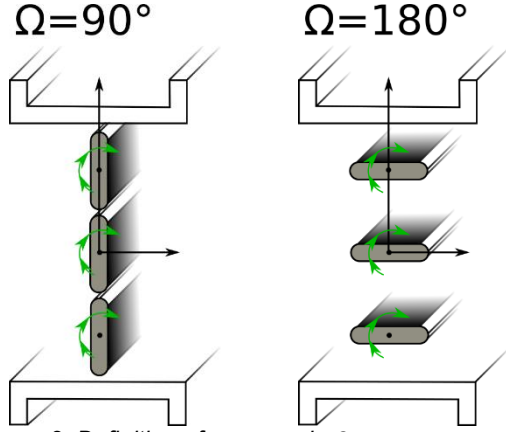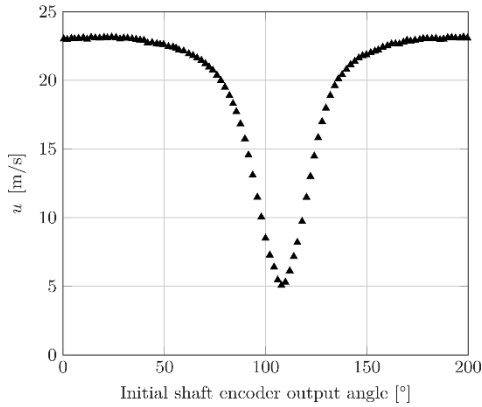
Ω=90°   Ω=180°

Figure 2: Definition of vane angle Ω

Figure 3: Reference run

In order to investigate the unsteady heat transfer, fluid temperatures as well as the surface temperature in the wake region of the vortex generator were measured. A FLIR SC7600 infrared camera with a measurement frequency of 16 Hz delivered spatially and temporally resolved surface temperature data. Therefore, a CaF_2 window in the top wall of the channel provided an optical access with a transmittance above 95 % in the spectral range of the infrared camera (1.5 μm - 5.1 μm). Additionally a black paint coating of the plate increased the emittance and reduced the influence of the radiation of the surrounding on the measurement signal of the infrared camera. Further details of the influence of surrounding radiation and a radiation balance are given in Brack et al. [18].

An influence of the overall thermal situation on the measurement data of the infrared camera is avoided by an in situ calibration with a surface thermocouple. The type T Omega CO-2 surface thermocouple is 0.013 mm thick and glued on a Perspex cylinder which is placed in a cylindrical sensor mount in the field of view.

Type T fine wire thermocouples with a wire diameter of 0.08 mm measured the fluid temperature at three positions in front and three positions downstream the vortex generator. The measuring tips of the thermocouples are located 0.03 m above the plate. All thermocouple signals were recorded
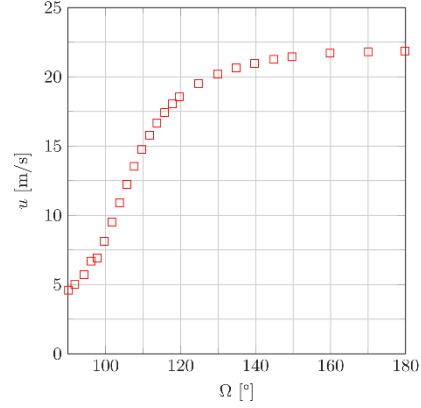
Figure 4: Relationship between u and Ω

with an I.E.D thermocouple measuring unit combining a thermocouple amplifier and a NI-USB6218 data acquisition device. The measurement uncertainty of the thermocouples was reduced to 0.2 K by a stationary calibration with an AMETEK RTC-159B dry block calibrator.

One key factor for the correct evaluation of the unsteady heat transfer is the data acquisition of the different devices on the same time base. Therefore, a Vellemann K8061 interface board triggered all measurement devices. The measurement frequency of the NI data acquisition devices was set to 4 kHz.

The operating range of the experimental setup describes the relationship between process variables (u, T_f) and the control variables (U_H, Ω). With a known operating range, the histories of the control variables can be calculated in advance, simplifying the controlling during the experiment.

Two hot wire probes at the test section inlet deliver the channel representative u and T_f used to control (see also Figure 1). A functional relationship

$$(u, T_f) = f(\Omega, U_H). \qquad (3)$$

between the local measurement (u, T_f) and the control variables is resolved by the stationary Bernoulli equation

$$p_\infty = p_C + \frac{1}{2} \rho_f u^2 \qquad (4)$$

and the stationary Energy equation

$$\dot{m}_f c_{p,f}(T_f - T_\infty) = P_H \qquad (5)$$
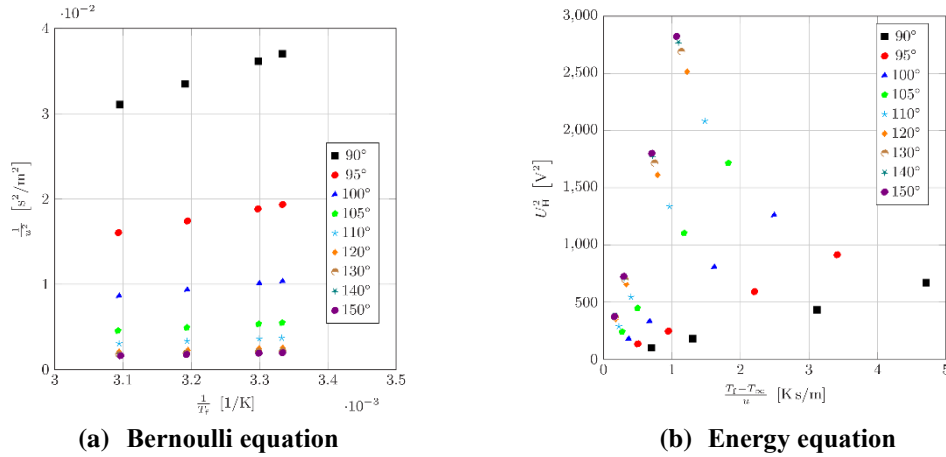
(a) Bernoulli equation

(b) Energy equation

Figure 5: Relationship between u, T_f, Ω and U

for an open system with a constant fluid mass flow $\dot{m}_f$ and a heater power input P_H. Both Eqns. (4) and (5) connect the ambient conditions of velocity $u_\infty = 0$ m/s, temperature T_∞ and static pressure p_∞ in the surrounding of the experimental setup with the conditions inside the test section (static pressure p_C, u and T_f).

Rewriting the system of equations with the aid of Ohm's law

$$P_H = \frac{U_H^2}{R_H} \qquad (6)$$

and the ideal gas law

$$p = \rho \mathfrak{R} T \qquad (7)$$

leads to the approximative relationships

$$\frac{1}{u^2} \approx f\left(\frac{1}{T_f}\right), \quad \Omega = \text{konst.} \qquad (8)$$

$$\frac{T_f - T_\infty}{u} \approx f(U^2), \quad \Omega = \text{konst.} \qquad (9)$$

for constant vane angles. While R_H represents the constant heater mess resistance, $\mathfrak{R}$ is the ideal gas constant for dry air.

In Figures 4 (a) and (b), the measured values of u and T_f are plotted against the set values of U_H and Ω according to the relationships given in Eqns. (8) and (9). The measurement data suggests a linear modelling of both Eqns. (8) and (9). The regression based constants are dependent on Ω and only valid for one set of a constant rotational speed of the root pump and a valve position of the bypass channel.

The boundary velocity profiles characterize the flow at the inlet region of the test section. By varying Ω during the experiment, also the inlet velocity profiles change. Therefore, the velocity profiles in z-direction were measured for different Ω. Moreover, the traversing delivered a local measurement

position with a flow velocity equal to the average inlet velocity $\bar{u}$.

Figure 6 shows the velocity profiles for seven different Ω, normalized with $\bar{u}$ and measured at the center of the channel. The non symmetrical shape of the profiles is independent of Ω. Also the shape of the boundary layer profiles at the bottom wall and the top wall is different. One reason are the boreholes in the top wall which are necessary as probe ports.

Independent of Ω, at $z = 0.02$ m the local u is equal to the average velocity $\bar{u}$. Therefore, this measurement position was used to characterize the inlet flow conditions during the experiments presented in the section RESULTS.

Besides the shown velocity profiles in Fig. 6, other measurements were made. One measurement series was performed at $\Omega = 220\,°$. Furthermore, two other measurement series at different y positions ($y = +0.06$ m and $y = -0.06$ m) to characterize the flow over the entire cross section were made. All measured profiles showed the same shape as in Fig. 6.
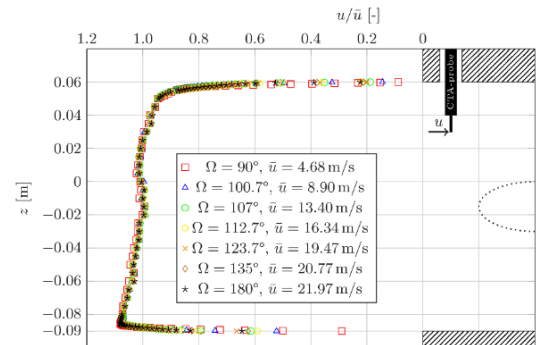

Figure 6: Inlet velocity profiles for different vane angles Ω normalized with the average velocity $\bar{u}$

Based on the theory of an isotropic turbulence, the hot wire measurements yielded an average freestream turbulence

83

$$\overline{\mathrm{Tu}} = \frac{1}{N} \sum_{i=1}^{N} \frac{\sigma_{u_i}}{u_i} \qquad (10)$$

dependent on the Reynolds number $\mathrm{Re} = \bar{u}\rho d/\eta$. It was calculated with the average velocity $\bar{u}$ and the hydraulic diameter d of the inlet section.

Figure 7 shows the relationship between $\overline{\mathrm{Tu}}$ and Re varying between 0.3 % and 1.2 %.
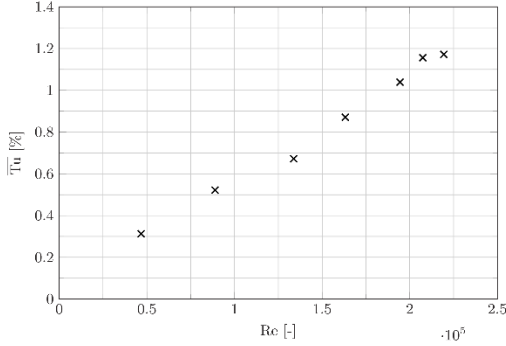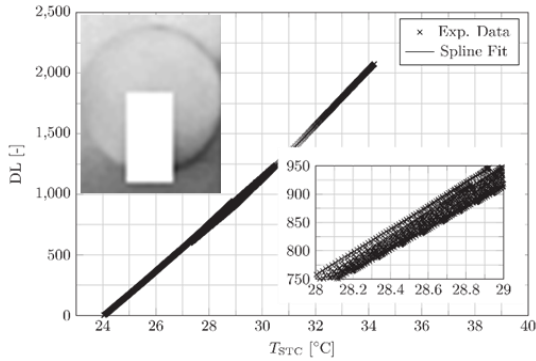

Figure 7: Relationship between the freestream Turbulence $\overline{Tu}$ and the Reynolds number Re

The results are independent of the emittance, as the surface thermocouple and the Perspex are coated with black paint.

Assigning the correct pixels to the thermocouple response T_{STC} is done with an evolution algorithm evaluating the measurement data of a pulsing fluid temperature experiment. Storn et al. [19] derived the applied evolution algorithm. As more than one pixel represents the surface thermo-
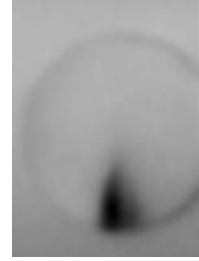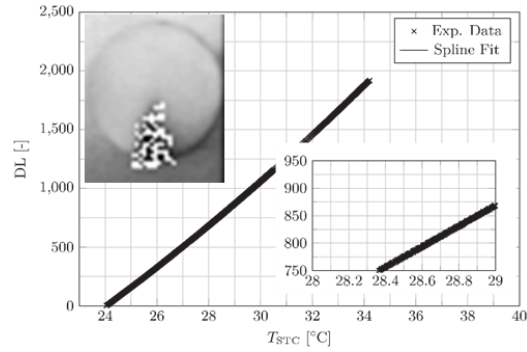

Figure 8: Infrared image of the surface thermocouple glued on the Perspex cylinder

(a) Initial assignment

(b) Optimized assignment

Figure 9: Allocation of pixels representing the surface thermocouple response

In summary, the experimental setup with its electric throttle mechanism delivers deterministic results concerning the flow pattern. Moreover, the measured profiles could be used as inlet profiles for numerical simulations. A measurement position where the current velocity represents the average velocity is at $z = 0.02$ m. For the experimental results discussed in the section RESULTS the position of the hotwire probes was kept constant.

The in situ calibration of the infrared camera is performed with a surface thermocouple glued on top of a Perspex cylinder and located in top right corner of the field of view. Figure 8 shows a greyscale infrared image of the Perspex cylinder during the experiment. The infrared image visualizes that the thermocouple wires are running on the top surface of the cylinder from below to the center. The differences in greyscale/temperature are a direct result of different material properties between the thermocouple and the Perspex around.

couple, the average value of the assigned pixels is used.

With increasing frequency and amplitude T_{STC} differ from the Perspex around it. This discrepancy is used to assign the correct pixels. Plotting the correctly assigned and averaged pixel response against T_{STC} leads to a single curve. In contrast, Figure 9 (a) shows the received relationship between infrared camera response (Digital level DL) and thermocouple response if pixels are included not representing the thermocouple. The picture in the top left corner of the plot visualizes the assigned white pixels. Between 28 °C and 31 °C the relationship is not represented by a single curve but fans out. Hence, the pixels do not accurately represent the thermocouple response.

Figure 9 (b) shows an optimized result for the assignment of pixels to the thermocouple response. The relationship is represented by a single curve and shifted to lower digital levels. With the aid of the evolution algorithm the best pixel in a user

defined region are chosen minimizing the quadratic deviation between a third order B-spline fit of the relationship and the chosen pixel values. Additionally applying a multi grid approach improves the convergence. First, pixels are clustered to bigger regions representing a coarser grid. Then, the evolution algorithm delivers the regions which fit best to the response. In the next step, only the best regions are divided into finer regions and optimized again. In the last step, only pixels and no regions any more are optimized.

EVALUATION METHOD

The heat transfer in the wake region of the vortex generator during temporally varying boundary conditions results in a three-dimensional and time-dependent heat conduction situation on the solid side. According to Carslaw and Jaeger [2], the heat conduction equation

$$\frac{\partial T_w}{\partial t} = a_w \left[\frac{\partial^2 T_w}{\partial x^2} + \frac{\partial^2 T_w}{\partial y^2} + \frac{\partial^2 T_w}{\partial z^2} \right] \quad (11)$$

describes such situations for materials with constant material properties ρ_w, c_w, k_w which are combined to the thermal diffusivity $a_w = k_w/(\rho_w c_w)$.

At the beginning of the experiment, the complete experimental setup is in thermal equilibrium leading to the initial condition

$$t = 0: \quad T_w = T_\infty . \quad (12)$$

Increasing then at a certain point in time the temperature of the fluid T_f leads to a heat flux into the wall expressed by the boundary condition

$$t > 0, z = 0: \quad k_w \frac{\partial T_w}{\partial z} = \dot{q}_s(x, y, t). \quad (13)$$

A method to evaluate such heat transfer situations was derived by Estorf [21] and is also applied for this publication. It is based on the analytical solution for an area-related heat release $2q_s(x, y, z = 0)$ in the xy-plane of an infinite solid. The corresponding initial condition

$$t = 0: \quad \theta_w = \frac{2q_s}{\rho_w c_w} \delta(z) \quad (14)$$

is expressed with a normalized temperature

$$\theta_w = T - T_\infty \quad (15)$$

and the Dirac-function $\delta(z)$. Substituting Eqn. (15) into the partial differential equation of Eqn. (11) and performing a Fourier transformation in space simplifies Eqn. (11) to an ordinary differential equation

$$\frac{\partial \tilde{\theta}_w}{\partial t} = -a_w (u^2 + v^2 + w^2) \tilde{\theta}_w \quad (16)$$

where u, v, w represent the frequencies to x, y, z. Solving Eqn. (16) and substituting Eqn. (14) one obtains the Fourier transform

$$\tilde{\theta}_w(u, v, z, t)$$
$$= \frac{1}{\rho_w c_w \sqrt{\pi a_w t}} q_s(u, v) e^{-a_w(u^2+v^2)t - \frac{z^2}{4a_w t}} \quad (17)$$

which is already transformed back in z.

Eqn. (17) represents the solution to an initial heat release. Applying the Duhamel's principle transforms Eqn. (17) to a solution of a time-dependent boundary condition which results in

$$\tilde{\theta}_w(u, v, z, t) = \frac{1}{\rho_w c_w \sqrt{\pi a_w}} \times$$
$$\int_o^t \dot{q}_s(u, v, \tau) e^{-a_w(u^2+v^2)(t-\tau) - \frac{z^2}{4a_w(t-\tau)}} d\tau \quad (18)$$

and represents the Fourier transform of θ_w to a time-dependent heat flux boundary condition.

Within the experiment, the surface temperature T_s is measured, while the surface heat flux $\dot{q}_s$ should be calculated. Therefore, it is necessary to invert Eqn. (18) which leads to

$$\dot{q}_s(u, v, t) = \frac{k_w}{\sqrt{\pi a_w}} \times$$
$$\int_o^t \frac{\partial \left[\tilde{\theta}_w(u, v, z = 0, t) e^{-a_w(u^2+v^2)(t-\tau)} \right]}{\partial \tau} \quad (19)$$
$$\frac{1}{\sqrt{t - \tau}} d\tau.$$

The mathematical steps to calculate the inverse of Eqn. (18) are described by Estorf [21] in detail.

Using a piecewise linear approximation of the surface temperature history

$$t_i < \tau < t_{i+1}:$$
$$T_s(\tau) = \frac{T_s(t_{i+1}) - T_s(t_i)}{t_{i+1} - t_i} (\tau - t_i) \quad (20)$$
$$+ T_s(t_i),$$

Eqn. (19) simplifies to a finite sum
$$\dot{q}_{s,lm}^n$$
$$= k_w \sum_{k=0}^{n-1} \left\{ \left[\left(\frac{1}{2\omega_{lm} a_w} + \omega_{lm}(t_n \right. \right. \right.$$
$$\left. - t_k) \right) \frac{\tilde{\theta}_{lm,k+1} - \tilde{\theta}_{lm,k}}{\Delta t}$$
$$+ \omega_{lm} \tilde{\theta}_{lm,k} \right] (\mathrm{erf} \langle f_{lm}(t_k) \rangle \quad (21)$$
$$- \mathrm{erf} \langle f_{lm}(t_{k+1}) \rangle)$$
$$+ \frac{\tilde{\theta}_{lm,k+1} - \tilde{\theta}_{lm,k}}{\sqrt{\pi a_w} \Delta t} \left(\sqrt{t_n - t_k} e^{-a\omega_{lm}^2(t_n - t_k)} \right.$$
$$\left. \left. - \sqrt{t_n - t_{k+1}} e^{-a\omega_{lm}^2(t_n - t_{k+1})} \right) \right\}.$$

The discrete frequencies u_l and v_m are substituted with the frequency $\omega_{lm} = \sqrt{u_l^2 + v_m^2}$ and the function $f_{lm}(\tau) = \omega_{lm} \sqrt{a_w(t_n - \tau)}$.

In order to apply Eqn. (21) as evaluation equation, it is necessary to transform the first normalized temperature into Fourier space. Reducing the transformation to a cosine transformation results in adiabatic boundaries for the region of interest.

The semi-infinite wall assumption limits the duration t_d of the experiment depending on the material properties and the plate thickness L. Schultz and Jones [22] derived a criterion in order to ensure the compliance of the semi-infinite wall assumption for the given conditions. They applied the analytical solution for a one-dimensional heat conduction situation with a constant surface heat flux and accepted a heat flux in the penetration depth less than 1 % of the surface heat flux. As their criterion is very severe, Vogel and Weigand [23] expanded the criterion of Schultz and Jones to

$$t_d < \frac{1}{4}\left[\frac{L}{2}\right]^2 \frac{\rho_w c_w}{k_w} = 518 \text{ s} . \qquad (22)$$

This criterion ensures a deviation in the calculated heat transfer coefficient less than 1 % compared to the analytical solution for a finite substrate with a step change in the reference temperature and a one-dimensional heat conduction situation.

RESULTS

In the following section, the results of two different experiments are presented and discussed. First, an unsteady heat transfer experiment with a constant fluid velocity $u = 15$ m/s and a fluid temperature S-shaped increase from ambient conditions to 35 °C. After reaching the temperature of 35 °C, T_f started a sinusoidal pulsation with an amplitude of 11 K and a frequency of 0.1 Hz. Below, this experiment is named Experiment A.

During the second presented unsteady heat transfer experiment the fluid velocity pulsated sinusoidal with an amplitude of 5 m/s and a frequency of 0.1 Hz around the mean velocity of 15 m/s. Meanwhile the fluid temperature increased with an S-shape from ambient conditions to 40 °C. Below, this experiment is named Experiment B.

Experiment A (T_f pulsation)

Figure 10 (a) shows the temporal set point variation of u and T_f defined before the experiment. With the experimentally determined operational range, described in section EXPERIMENTAL SETUP, it was possible to calculate the heater voltage U_H history and the vane angle Ω history in advance.

As u is kept constant, the necessary variations of the vane angle are in the range of 2°. Further Fig. 10 (b) visualizes the nonlinear dependence between (u, T_f) and (U_H, Ω). The sinusoidal pulsation of T_f requires a non-sinusoidal pulsation of U_H and Ω becoming apparent with the different shapes of the maxima and the minima.

Figure 10 (c) represents the measured u and T_f history. The fluid velocity is kept almost constant and deviates from the constant value less than 0.3 m/s. The measured T_f shows an initial positive offset to the set point value. This offset is a result of an increased ambient temperature between the point in time of the determination of the operational range and the point in time of the performed experiment. Furthermore, the measured amplitude of the T_f pulsation is a little bit smaller than the defined one. This damping effect results from transient effects not considered with the stationary determination of the operational range.

Figure 10 (d) and (e) show the Fast Fourier amplitude spectra of T_f as well as u and were calculated with the measured signal between 60 s and 180 s. The amplitude spectra for T_f has a sharp maxima at 0.1 Hz. The value of amplitude of the first harmonic at 0.2 Hz is 37 times smaller. The amplitude spectra of u is almost zero apart from the amplitude at 0 Hz representing the mean value.

The calculated surface heat flux histories are plotted in Fig. 10 (f) for three different evaluation positions. Figure 10 (h) visualizes the evaluation positions with an infrared greyscale image at $t = 60$ s. White regions represent higher surface temperature values than darker ones. Independent of the T_f pulsation, the infrared image visualizes the heat transfer pattern in the wake region of the vortex generator. Two streaks of high heat transfer leading to higher surface temperatures and a valley of low heat transfer in between on each side.

As a result of the logistic growth of the fluid temperature towards a constant value of 35 °C, $\dot{q}_s$ increases, reaches a local maximum and then starts to decrease (Pos. 0) or keeps nearly constant (Pos. 1, Pos. 2). The subsequent pulsations of T_f propagates to $\dot{q}_s$. The surface heat flux $\dot{q}_s$ pulsates with the same frequency and measured amplitude of 11 K leads to temporal reversal of $\dot{q}_s$.

The local heat transfer coefficient histories, plotted in Fig, 10 (g), are obtained from Eqn. (1) using the calculated $\dot{q}_s$, the measured T_s and the locally interpolated T_f. With increasing T_f after $t \approx 17$ s the surface heat flux increases and a heat transfer coefficient can be calculated. As the temperature differences between T_f and T_s are initially rather small, the calculated heat transfer coefficients tend to infinity. With increasing evaluation time the temperature difference $T_f - T_s$ increases and the heat transfer coefficients reach almost constant values as long as T_f does not pulsate. During the subsequent T_f pulsation, the heat transfer coefficients vary. When T_f and T_s intersect, h tends to $\pm\infty$.

Experiment B (u pulsation)

In contrast to experiment A, the fluid velocity pulsates and the fluid temperature increases from ambient conditions to a constant value of 40 °C

during experiment B. Figure 11 (a) visualizes the defined set point histories of u and T_f. Compared to the vane angle history of experiment A (Fig. 10 (b)), for experiment B the variations are obviously larger (Fig. 11 (b)). Figure 11 (c) shows the measured histories of u and T_f. The amplitude of the measured u is a little bit larger than for the defined set point values. Especially in the range of the minima, the measured u falls below the set point. This is a result of the time lag of the electric motor in combination with the stronger sensitivity of the throttle mechanism for smaller Ω (Fig. 4).

The measured T_f shows on the one hand a positive offset of the initial value to the set point value. On the other hand T_f is not constant for the higher temperature level. It varies with the pulsation of u and is phase shifted. The fluid temperature T_f reaches local maxima during local minima of u, but the pulsation amplitude of T_f is less than 1 K.

The plotted Fast Fourier amplitude spectra of Fig. 11(c) and (d) are calculated with the corresponding signal between 40 s and 140 s. Both amplitude spectra show a sharp maximum for $f = 0.1$ Hz. The amplitude of the first, second and third harmonic is visible but significantly smaller than fundamental frequency. The maxima of the velocity amplitude spectra are a bit broader than for T_f.

A comparison of the local heat flux histories of experiment A and B (Figures 10 (f) and 11 (f)) shows different trends. The T_f pulsation during the experiment A influences the heat flux globally and leads to pulsation at every position. However, the amplitude of the heat flux pulsation varies locally.

The heat flux during the experiment B (u pulsation) behaves different at each position. For Pos. 0 the decrease of $\dot{q}_s$ is superimposed with a pulsation showing a fast increase phase followed by a significantly slower decrease phase. In spite to Pos. 0, $\dot{q}_s$ at Pos. 2 is superimposed by a sinusoidal pulsation. The pulsations of the heat flux at Pos. 1 exhibits broad minima and sharp maxima. Further for later points in time, $\dot{q}_s$ at Pos. 1 temporally exceeds $\dot{q}_s$ at Pos. 0. The differences between the three different evaluation positions indicate a varying influence of changes in the fluid velocity on the heat transfer.

Figure 11 (g) includes the histories of the calculated heat transfer coefficients at the different evaluation positions. All h histories show a pulsating behavior. Up to $t = 100$ s, the moving average of h at Pos. 0 decreases while it is constant for Pos. 1 and Pos. 2. The broader minima and sharper maxima, already seen for $\dot{q}_s$, appear also for h at Pos. 1.

CONCLUSION

This paper presents and characterizes an experimental setup to control and vary the fluid temperature and the fluid velocity independently during unsteady heat transfer experiments. The multi variable control system is realized by the simultaneous control of an electric throttle mechanism and a mesh heater. A stationary determination of the operational range delivers the dependences between the control variables heater voltage and vane angle and the output quantities fluid velocity and fluid temperature. In addition, the inlet flow conditions are investigated by traversing hot wire probes to measure the fluid velocity profile.

The presented system works well for variations of the fluid temperature and a constant fluid velocity. Such kind of experiments mainly require changes of the heater voltage. As the influence of a varying fluid temperature is weak on the velocity, only small changes of the vane angle are required.

For experiments with varying fluid velocity and constant fluid temperature in parts, the variation of fluid velocity requires also significant variations of the heater voltage under some circumstances. Therefore, deviations of the current fluid temperature from the set point arise dependent on the frequency and the amplitude of the velocity changes. In order to improve the accuracy of the experimental setup, the consideration of transient effects and an electric motor with a faster response time would be necessary.

A high accuracy is achieved for pulsating processes. The amplitudes of the nth harmonic are significantly smaller than the amplitude of the required fundamental frequency.

Besides the experimental setup, an approach to improve the accuracy of the in situ calibration of the applied infrared camera is discussed. The results of an experiment with pulsating fluid temperature and constant fluid velocity are applied to localize the surface thermocouple in the field of view of the infrared camera. The method delivered improved results compared to the manual selection of pixels representing the thermocouple response.

The evaluation of the experiments is carried out with the measurement of surface temperatures, fluid temperatures, the fluid velocity and the calculation of the surface heat flux. The calculation of surface heat flux with the evaluation method derived by Estorf [21] considers lateral heat conduction. Hot wire probes deliver local measurements of the fluid velocity.

REFERENCES

[1] Rolls Royce, plc.; 2015. The jet engine, John Wiley & Sons.

[2] Zudin, Y. B.; 2007. "Theory of periodic conjugate heat transfer", Springer Berlin Heidelberg, pp. 1-226.

[3] Mathie, R.; Markides, C.N.; 2013. "Heat transfer augmentation in unsteady conjugate thermal systems–Part I: Semi-analytical 1-D framework", Int. J. of Heat and Mass Transfer, 56(1-2), pp. 802-818.

[4] Mathie, R.; Nakamura, H.; Markides, C.N.; 2013. "Heat transfer augmentation in unsteady conjugate thermal systems–Part II: Applications", Int. J. of Heat and Mass Transfer, 56(1-2), pp. 819-833.

[5] Ekkad, S. V.; Ou, S.; Rivir, R. B.; 2006. "Effect of jet pulsation and duty cycle on film cooling from a single jet on a leading edge model", J. of Turbomachinery, 128(3), pp. 564-571.

[6] Dec, J. E.; Keller, J. O.; 1989. "Pulse combustor tail-pipe heat-transfer dependence on frequency, amplitude, and mean flow rate", Combustion and Flame, 77(3-4), pp. 359-374.

[7] Ishino, Y.; Suzuki, M.; Abe, T.; Ohiwa, N.; Yamaguchi, S.; 1996. "Flow and heat transfer characteristics in pulsating pipe flows (effects of pulsation on internal heat transfer in a circular pipe flow)", Heat Transfer-Japanese Research: Co-sponsored by the Society of Chemical Engineers of Japan and the Heat Transfer Division of ASME, 25(5), pp. 323-341.

[8] Barker, A. R.; Williams, J. E. F.; 2000. "Transient measurements of the heat transfer coefficient in unsteady, turbulent pipe flow", Int. J. of Heat and Mass Transfer, 43(17), pp. 3197-3207.

[9] Liu, C.; von Wolfersdorf, J.; Zhai, Y.; 2014. "Time-resolved heat transfer characteristics for steady turbulent flow with step changing and periodically pulsating flow temperatures", Int. J. of Heat and Mass Transfer, 76, pp. 184-198.

[10] Liu, C.; von Wolfersdorf, J.; Zhai, Y.; 2014. "Time-resolved heat transfer characteristics for periodically pulsating turbulent flows with time varying flow temperatures", Int. J. of Thermal Sciences, 89, pp. 222-233.

[11] Liu, C.; von Wolfersdorf, J.; Zhai, Y.; 2015. "Comparison of time-resolved heat transfer characteristics between laminar and turbulent convection with unsteady flow temperatures", Int. J. of Heat and Mass Transfer, 84, pp. 376-389.

[12] Janetzke, T.; Nitsche, W.; Täge, J.; 2008. "Experimental investigations of flow field and heat transfer characteristics due to periodically pulsating impinging air jets", Heat and Mass Transfer, 45(2), pp. 193-206.

[13] Sheriff, H. S.; Zumbrunnen, D. A.; 1994. "Effect of flow pulsations on the cooling effectiveness of an impinging jet", J. of Heat Transfer, 116(4), pp. 886-895.

[14] Camci, C.; Herr, F.; 2002. "Forced convection heat transfer enhancement using a self-oscillating impinging planar jet", J. of Heat Transfer, 124(4), pp. 770-782.

[15] Hofmann, H. M.; Movileanu, D. L.; Kind, M.; Martin, H.; 2007. "Influence of a pulsation on heat transfer and flow structure in submerged impinging jets", Int. J. of Heat and Mass Transfer, 50(17-18), pp. 3638-3648.

[16] Coulthard, S. M.; Volino, R. J.; Flack, K. A.; 2007. "Effect of jet pulsing on film cooling—part I: effectiveness and flow-field temperature results", J. of Turbomachinery, 129(2), pp. 232-246.

[17] Henze, M.; von Wolfersdorf, J.; Weigand, B.; Dietz, C.F.; Neumann, S. O.; 2011. "Flow and heat transfer characteristics behind vortex generators–A benchmark dataset", Int. J. of Heat and Fluid Flow, 32(1), pp. 318-328.

[18] Brack, S.; Poser, R.; von Wolfersdorf, J.; 2017. "A comparison between transient heat transfer measurements using TLC and IR thermography", Proceedings of ExHFT-9, Iguazu Falls (Brazil).

[19] Storn, R.; Price K.; 1997. "Differential evolution – a simple and efficient heuristic for global optimization over continuous spaces", J. Global Optim. 11(4), pp. 341-359.

[20] Carslaw, H. S.; Jaeger, J. C.; 1959. "Conduction of heat in solids", Oxford: Clarendon Press.

[21] Estorf, M. 2005. "Image based heating rate calculation from thermographic data considering lateral heat conduction", Int. J. of Heat and Mass Transfer, 49(15-16), pp. 2545-2556.

[22] Schultz, D.L.; Jones, T.; 1973. "Heat-transfer measurements in short-duration hypersonic facilities", DTIC Document AGARD-AG 165

[23] Vogel, G.; Weigand B.; 2001. "A new evaluation method for transient liquid crystal experiments", National Heat Transfer Conference 2001 California, NHTC2001-20250
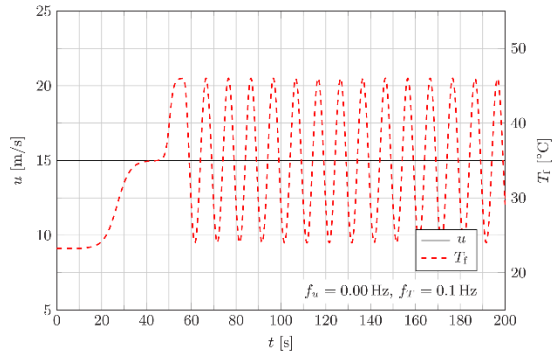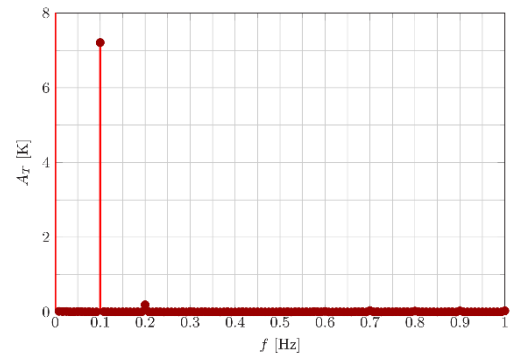
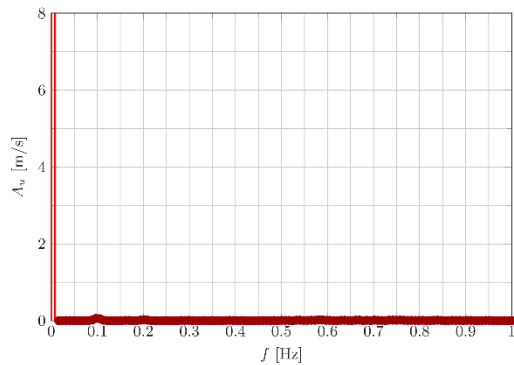**(a) Set point variation of flow velocity and flow temperature**
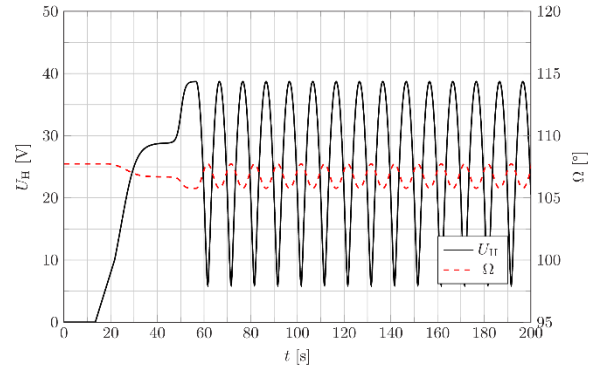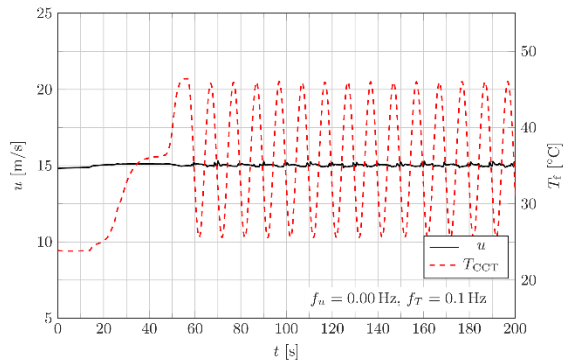
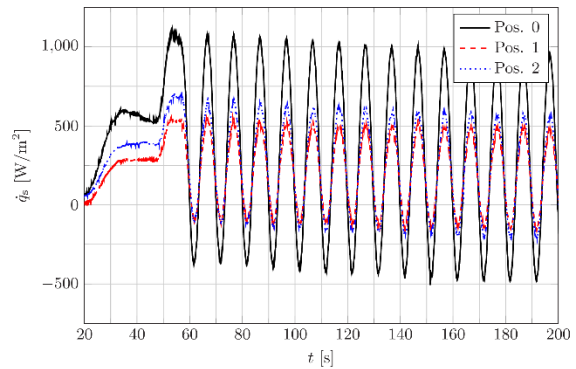**(b) Calculated heater voltage and vane angle history**
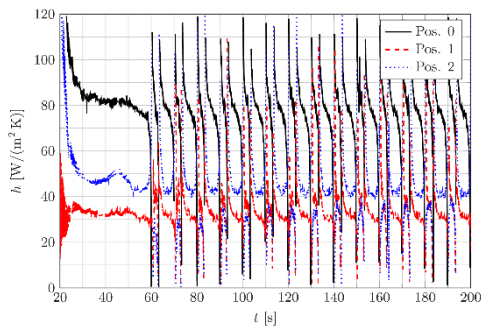

(c) Measured flow velocity and flow temperature
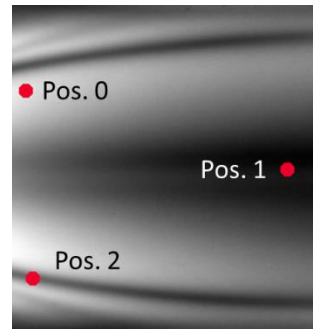

(d) FFT amplitude spectra of the fluid temperature

(e) FFT amplitude spectra of the fluid velocity
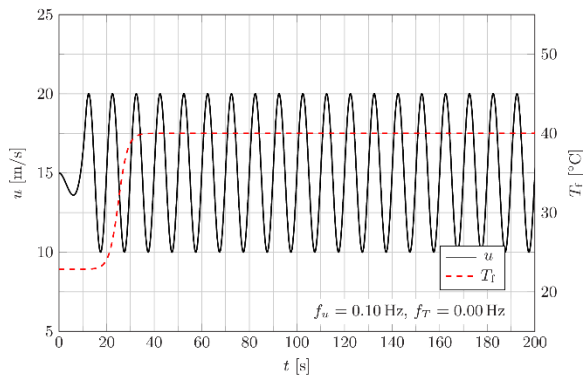

(f) Local surface heat flux histories
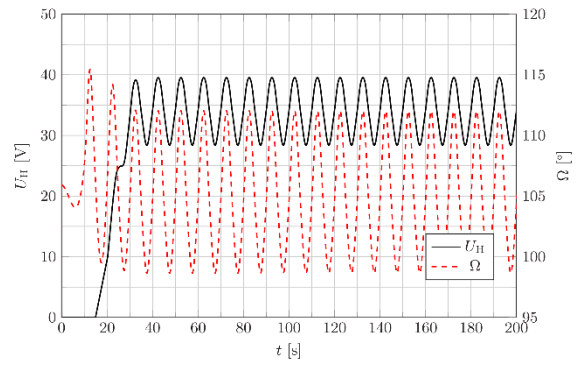

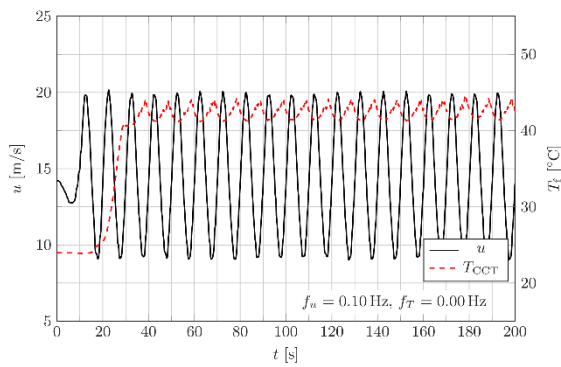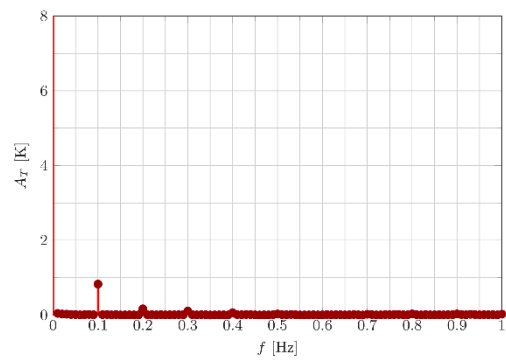**(g) Local heat transfer coefficient histories**

(h) Evaluation positions

Figure 10: Experimental results for a fluid temperature pulsation case ($f_T = 0.1\ Hz$) – Experiment A
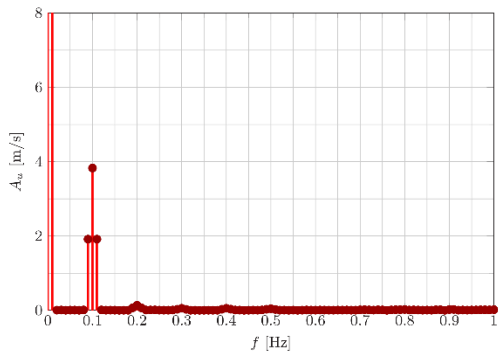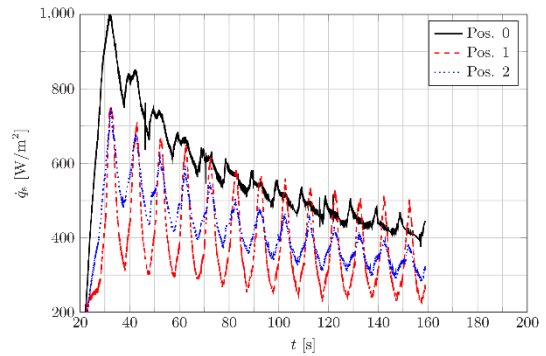
(a) **Required flow velocity and flow temperature**

(b) **Calculated heater voltage and vane angle history**

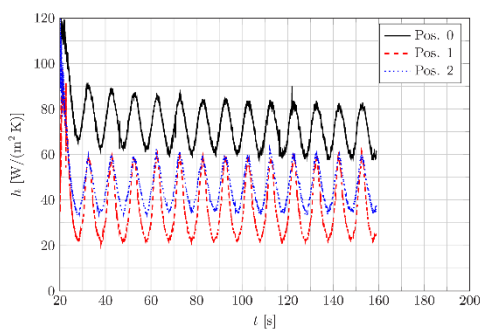(c) **Measured flow velocity and flow temperature**

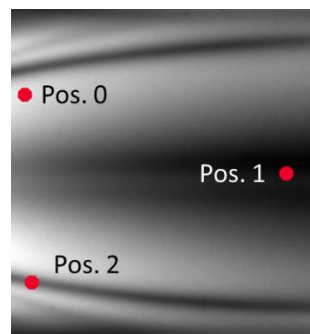(d) **FFT amplitude spectra of the fluid temperature**

(e) **FFT amplitude spectra of the fluid velocity**

(f) **Local surface heat flux histories**

(g) **Local heat transfer coefficient histories**

(h) **Evaluation positions**

Figure 11: Experimental results for a fluid velocity pulsation case ($f_u = 0.1\,Hz$) – Experiment B